

Joule heating-driven ultrafast synthesis of $(\text{Fe}_{1-x}\text{Mn}_x)_2\text{AlB}_2$ and its electromagnetic wave absorption properties

Yuhang Bai ^{1,2}, Zelong Yao ¹, Yang Yang ¹, Jinrui Li ¹, Jia Liu ¹, Peipei Wang ¹, Huiling Du ¹, Xing Zhao^{1,✉}, Laifei Cheng^{2,✉}

¹ *School of Material Science and Engineering, Xi'an University of Science and Technology, Xi'an 710054, China*

² *Science and Technology on Thermostructural Composite Materials Laboratory, Northwestern Polytechnical University, Xi'an 710072, China*

✉ Corresponding authors.

E-mail: X. Zhao, zhaoxing@xust.edu.cn;

L. Cheng, chenglf@nwpu.edu.cn

Received: January 6, 2025; Revised: February 25, 2025; Accepted: February 26, 2025

© The Author(s) 2025.

Abstract: Defect engineering enables the efficient management of electromagnetic parameters and the enhancement of electromagnetic wave (EMW) absorption. In this study, $(\text{Fe}_{1-x}\text{Mn}_x)_2\text{AlB}_2$ transition metal boride (MAB) phases with a layered structure were prepared via Joule heating-driven ultrafast synthesis, and their EMW absorption properties were investigated. The experimental

results demonstrate that the incorporation of Mn atoms at the M site can effectively modulate the impedance matching and EMW absorption properties of the material through the introduction of defects, such as defects and lattice distortions. Notably, $(\text{Fe}_{0.3}\text{Mn}_{0.7})_2\text{AlB}_2$ exhibits a reflection loss as high as -47.8 dB at 12.24 GHz, with a maximum effective absorption bandwidth of 4.16 GHz (10.24–14.40 GHz) at an ultrasmall thickness of 1.5 mm. This study provides a promising avenue for the development of excellent microwave-absorbing materials, which are essential for meeting the evolving requirements of advanced electronics. Additionally, this work offers a paradigm for enhancing other properties of MAB phases through defect engineering.

Keywords: Electromagnetic wave absorption, Defect engineering, Joule heating-driven ultrafast synthesis, Transition metal boride phases.

1 Introduction

The ubiquitous exposure to electromagnetic wave (EMW) resulting from the proliferation of electronic devices poses significant implications for human health [1-3]. Consequently, there is an increasing demand for EMW-absorbing materials exhibiting broadband performance, strong EMW absorption, and lightweight properties to address this issue and perform multiple functionalities [4]. Transition metal boride (MAB) phases, which comprise a transition metal element (M), a group-A element (IIIA and IVA), and boron (B), exhibit good physicochemical properties, such as a high electrical and thermal conductivity, as well as a nano-lamellar microstructure [5]. The combination of these attributes makes MAB phases exceptionally promising candidates for microwave absorption applications [6].

Fe_2AlB_2 , a typical MAB phase, exhibits considerable potential as an effective wave-absorbing material due to its low density ($5.57 \text{ g}\cdot\text{cm}^{-3}$), metal-like electrical conductivity, ferromagnetic properties, and magnetothermal effect [7-10]. However, its magnetic loss capacity is relatively

limited, which hampers its wave absorption ability. To address this, the deliberate incorporation of magnetic elements (such as Fe, Co, Ni, and Mn) through doping has been proposed as a strategy to maintain the excellent dielectric properties of the material while simultaneously enhancing its magnetic loss, thereby improving its overall ability to absorb EMW—a concept that has been successfully applied to various materials. For instance, Luo et al. increased the charge density around the M-site atoms of Ti_2AlC by introducing defects through V and Cr doping. This variation in the charge density favors the formation of dipoles, with the dipole strength increasing with the amount of V or Cr added, thus enhancing the polarization loss of the material. The sample prepared via this approach had a minimum reflection loss (RL_{\min}) of -56.2 dB and good EMW absorption properties [11]. Similarly, Li et al. doped the M site of Ti_3AlC_2 with Fe, which resulted in a significantly enhanced magnetic loss due to the introduction of both magnetic components and defects. The layered Ti_3AlC_2 structure and coexisting phases expand the active interface, enhancing the local polarization and improving the microwave absorption capabilities of the material. Thanks to the combined effects of dielectric and magnetic losses, the resulting Fe-doped Ti_3AlC_2 possessed an RL_{\min} of -33.3 dB [12]. Using a similar strategy, Han et al. introduced defects by doping the M site of V_2AlC with magnetic elements (Fe, Co, Ni, and Mn). The addition of these magnetic elements expanded the non-uniform interface between the high-entropy MAX phase (X is carbon or nitrogen) and paraffin wax, enhancing the interfacial polarization. The natural resonance and eddy current losses due to the incorporation of magnetic elements endowed the material with effective magnetic losses and improved impedance matching, resulting in an RL_{\min} of -37.4 dB [13]. Given the structural similarities between the MAX and MAB phases, it is believed that the same doping approaches can be applied to MAB phases. Thus, optimizing the magnetic loss capability of Fe_2AlB_2 through M-site doping with magnetic elements has become a research hotspot for enhancing its wave-absorption performance.

The incorporation of Mn at the M site appears to be an effective way to enhance the magnetic loss

of Fe_2AlB_2 . Mn_2AlB_2 shows antiferromagnetic ordering below a Néel temperature (T_N) of 313 K [14]. The antiferromagnetic properties of Mn_2AlB_2 allow it to interact with Fe_2AlB_2 , which displays ferromagnetic characteristics. This interaction results in a magnetization jump, which is typically accompanied by a significant change in the saturation magnetization [14]. Melikhov et al. studied the effect of Mn doping and the adjustment of the Fe–Mn atomic ratio on the magnetic anisotropy of $\text{CoMn}_x\text{Fe}_{2-x}\text{O}_4$ ferrites and concluded that Mn doping reduces the magnetic anisotropy of the ferrite crystals [15]. The reduction in the magnetic anisotropy of these crystals leads to a shift in their natural resonance frequency, which in turn causes an increase in natural resonance loss upon approaching the working frequency [16]. Furthermore, Shiotani et al. developed $(\text{Fe}_{1-x}\text{Mn}_x)_2\text{AlB}_2$ with coexisting ferromagnetic and antiferromagnetic states through Mn doping, and they reported that the direction of the magnetic moment of this system changed upon increasing the Mn concentration [14]. This change induces natural resonance loss when the direction of the magnetic moment aligns with the applied magnetic field as the magnetic domains gradually rotate. Therefore, incorporating Mn at the M site is an effective way to enhance the magnetic loss of Fe_2AlB_2 . Additionally, the ability to precisely adjust the Fe–Mn atomic ratio is a significant challenge that needs to be addressed.

Currently, MAB phases are typically prepared via powder solid-phase reaction sintering at high temperatures in muffle or tube furnaces. This method presents several disadvantages, including a slow temperature rise, the volatilization of the material elements, and the inhomogeneous composition (due to segregation) of the obtained materials [17]. The low heating rate leads to an increased grain size, which reduces the number of interfaces and defects within the material [18]. These interfaces and defects are crucial for EMW scattering and absorption [19]. Therefore, developing a rapid heating methodology that can be used to prepare MAB phases with suitable wave-absorption performance is urgently required. Joule heating-driven ultrafast synthesis is notable for its high heating (10^3 – 10^4 °C/min) and cooling (10^4 °C/min) rates, as well as the ability to reach

ultrahigh temperatures, up to 3000 °C. Such a high heating rate allows samples to quickly pass through the temperature range where only grain coarsening occurs, promoting grain refinement and consequently introducing more interfaces and defects. This method has also been shown to be effective for synthesizing a wide range of materials, such as BaTiO₃ and lead zirconate titanate (PZT) [20-22]. Therefore, it is reasonable to believe that this rapid preparation method can effectively shorten the sintering time, reduce element volatilization and unnecessary interdiffusion, and facilitate the precise tuning of the Fe–Mn atomic ratio.

In this work, (Fe_{1-x}Mn_x)₂AlB₂ samples ($x = 0, 0.2, 0.4, 0.5, 0.7$, and 1) were successfully prepared via Joule heating-driven ultrafast synthesis within 12 s at approximately 930 °C. The EMW absorption properties of the prepared materials and the associated dielectric and magnetic loss mechanisms were investigated. Mn doping introduces non-homogeneous interfaces and defects in Fe₂AlB₂, which results in high interfacial and dipole polarizations. Additionally, by optimizing the impedance matching through the synergistic effects of dielectric and magnetic losses, the EMW absorption capability of the material is enhanced. Notably, (Fe_{0.3}Mn_{0.7})₂AlB₂ exhibits a reflection loss as high as -47.8 dB at 12.24 GHz with a maximum effective absorption bandwidth (EAB_{\max}) of 4.16 GHz (10.24–14.40 GHz) at an ultrasmall thickness of 1.5 mm. This achievement can be attributed to the change in the magnetic moment and the occurrence of a super-magnetic jump at around $x = 0.7$, which enhances the saturation magnetization and magnetic loss of the material [14]. The present work demonstrates the significant potential of doping MAB phases with magnetic elements to modulate their dielectric and magnetic losses and thus enhance their wave-absorption properties. Furthermore, it provides a valuable reference for exploring the potential applications of other MAB phases as EMW absorbers.

2 Experimental materials and methods

2.1 Materials

High-purity commercial powders of Fe (99 wt%, 10 μm), B (99 wt%, 10–20 μm), Mn (99 wt%, 10 μm), and Al (99 wt%, 1 μm), as well as anhydrous ethanol, were obtained from Beijing InnoChem Science & Technology Co., Ltd. (Beijing, China). Carbon felt was purchased from Jiangxi Shuobang New Materials Technology Co., Ltd. (Jiangxi, China).

2.2 Synthesis of the $(\text{Fe}_{1-x}\text{Mn}_x)_2\text{AlB}_2$ powders

To prepare the $(\text{Fe}_{1-x}\text{Mn}_x)_2\text{AlB}_2$ samples, suitable quantities of the Fe, Mn, Al, and B powders were blended according to the stoichiometric ratios, that is $(\text{Fe}_{1-x}\text{Mn}_x):\text{Al}:\text{B} = 2:1:2$ (where $x = 0, 0.2, 0.4, 0.5, 0.7, \text{ and } 1$). Additionally, 10 wt% excess Al was incorporated into the mixture to compensate for potential Al volatilization. The mixtures were then subjected to wet ball milling using polytetrafluoroethylene (PTFE) jars, onyx balls, and ethanol as the grinding media. The wet ball milling process was conducted at 300 r/min for 12 h. Following milling, the material was dried in an oven at 60 $^{\circ}\text{C}$ for 10 h. Subsequently, 0.3 g of the dried powder was pressed into a cylindrical bulk with dimensions of $\phi 10 \times 3 \text{ mm}^2$ under a pressure of 30 MPa. The pressed billet was positioned centrally within a carbon felt, which measured 110 mm in length, 22 mm in width, and 5 mm in thickness. Afterwards, the carbon felt was affixed between the two end electrodes using a clamp. The electrodes were placed in a vacuum chamber and connected to a programmable DC power supply (PS91000-30, Elektro-Automatik, Germany) outside the chamber via a vacuum electrode. The vacuum chamber was sealed, and a mechanical pump was used to evacuate the chamber until the pressure dropped below 200 Pa. Sintering was carried out using a home-made Joule heating-driven ultrafast synthesis device (as shown in Fig. 1) [23-24], which was heated to $\sim 930 \text{ }^{\circ}\text{C}$ under vacuum conditions at a heating rate of $10^3\text{--}10^4 \text{ }^{\circ}\text{C}/\text{min}$. The sintering curves and sintering parameters of the $(\text{Fe}_{1-x}\text{Mn}_x)_2\text{AlB}_2$ powders are presented in Fig. S1 and Table S1, respectively. Following sintering, the power was turned off, the material was allowed to cool naturally to room temperature, and the complete sintered blocks were taken out of the chamber and pulverized into powder for further

analysis and utilization. The details of the preparation process of the $(\text{Fe}_{1-x}\text{Mn}_x)_2\text{AlB}_2$ powders are illustrated in the flowchart in Fig. 1.

2.3 Characterization

Phase structure analysis was carried out using an X-ray diffractometer (XRD, Bruker AXS D8 Advance, Germany) equipped with a Cu $K\alpha$ radiation source, and crystal structure analysis was performed via Rietveld refinement using the GSAS Rietveld software. The microstructure of the $(\text{Fe}_{1-x}\text{Mn}_x)_2\text{AlB}_2$ samples was investigated using field-emission scanning electron microscopy (SEM, QUANTA 250 FEG, FEI, USA) and transmission electron microscopy (TEM, Spectra 300, USA) in conjunction with energy-dispersive X-ray spectroscopy (EDX). The chemical state of the samples was investigated via X-ray photoelectron spectroscopy (XPS, Axis Ultra DLD). To investigate the magnetic properties of the $(\text{Fe}_{1-x}\text{Mn}_x)_2\text{AlB}_2$ samples, the room-temperature hysteresis loops were recorded to determine the saturation magnetization. A vibrating sample magnetometer (PPMS-VSM, LakeShore 7404, Columbus, OH, USA) was used for these measurements.

2.4 EMW absorption measurements

To evaluate the EMW absorption performance of the samples, each sample was mixed with paraffin in a mass ratio of 6:4. Subsequently, the mixture was pressed into a ring with an outer diameter of 7.0 mm, an inner diameter of 3.0 mm, and a thickness of 2.0–2.3 mm. The electromagnetic (EM) parameters of the prepared samples were measured using a vector network analyzer (VNA, AV3656D, China) in the frequency range of 2–18 GHz, employing the coaxial method.

3 Results and discussion

3.1 Characterization of the phase composition and microstructure

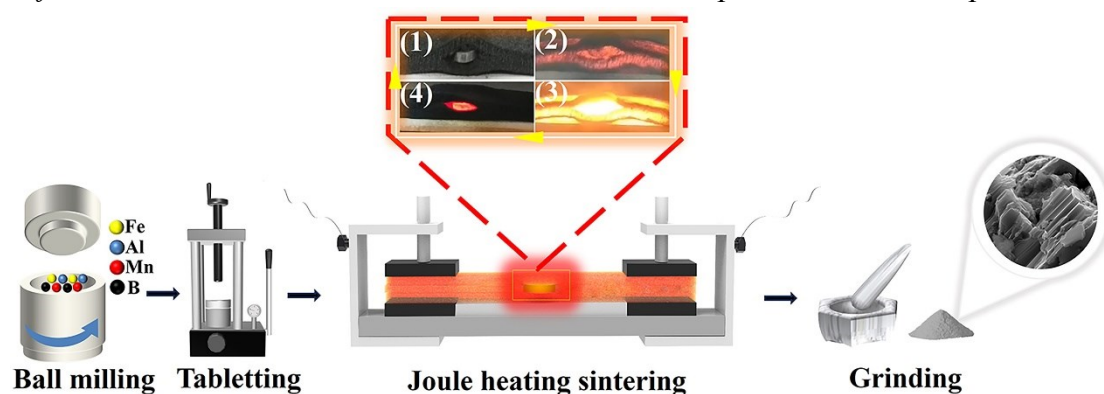


Fig. 1. Diagram illustrating the preparation process of the $(\text{Fe}_{1-x}\text{Mn}_x)_2\text{AlB}_2$ powders.

Fig. 1 illustrates the details of the preparation process of the $(\text{Fe}_{1-x}\text{Mn}_x)_2\text{AlB}_2$ powders. Here, the Joule heating process comprises four distinct stages. (1) Pre-sintering stage: The color of the carbon felt and the sample is the same. (2) Initial rapid heating stage: The carbon felt and the sample gradually turn red. (3) Intermediate stage with a slight temperature increase: The color of the carbon felt and the sample transitions from red to golden yellow. (4) Cooling stage: The carbon felt returns to its original black color, while the sample remains red. The red hue gradually dissipates as the sample cools to room temperature. The Joule heating-driven ultrafast synthesis method can achieve heating and cooling rates of up to 10^4 °C/min, which markedly enhances the efficiency of the preparation process in comparison to the conventional sintering method based on resistance heating (wherein the heating rate is typically less than 50 °C/min, and the cooling rate is approximately 5 °C/min).

Fig. 2(a) presents the XRD patterns of the $(\text{Fe}_{1-x}\text{Mn}_x)_2\text{AlB}_2$ samples with $x = 0, 0.2, 0.4, 0.5, 0.7$, and 1. Notably, the diffraction peaks of the parent phases in the $x = 0$ and $x = 1$ samples align precisely with the reference patterns PDF#04-007-5354 (Fe_2AlB_2) and PDF#97-002-5518 (Mn_2AlB_2), respectively. For Mn-doped samples ($x = 0.2-0.7$), the primary diffraction peaks progressively shift between the characteristic peaks of Fe_2AlB_2 and Mn_2AlB_2 . The observed intermediate diffraction peak position can be attributed to the difference in atomic radius between Mn and Fe, which induces systematic variations in the lattice parameters. Minor by-products are detected in all synthesized samples. Specifically, the XRD pattern of the pristine Fe_2AlB_2 ($x = 0$) reveals distinct peaks at $2\theta =$

22.43°, 26.66°, 43.01°, and 44.18°, corresponding to the (003), (022), (332), and (025) planes of the intermetallic compound $\text{Fe}_4\text{Al}_{13}$. The presence of $\text{Fe}_4\text{Al}_{13}$ can be attributed to the partial decomposition of Fe_2AlB_2 , facilitated by enhanced Al-Fe interactions under high-temperature synthesis conditions [25]. Similar $\text{Fe}_4\text{Al}_{13}$ signatures persist across $x = 0.2$ - 0.7 samples. Additionally, Mn doping introduces additional peaks at $2\theta = 37.42^\circ$, 40.93° , and 47.20° , which index to the (011), (111), and (102) planes of the $(\text{Fe}_{0.4}\text{Mn}_{0.6})\text{B}$ phase. These features confirm partial Mn incorporation into the Fe sublattice during synthesis [26]. In the sample with $x = 1$, the diffraction peaks observed at $2\theta = 26.80^\circ$, 37.15° , 38.97° , 40.60° , 44.55° , and 46.73° correspond to the (101), (011), (201), (111), (210), and (102) crystallographic planes of the MnB phase, respectively. Consequently, the previously identified $(\text{Fe}_{0.4}\text{Mn}_{0.6})\text{B}$ phase disappears, while MnB emerges as the dominant secondary phase [26]. Notably, the formation of boride- and intermetallic-based secondary phases is thermodynamically inevitable during the synthesis of MAB phases [25]. Intriguingly, these by-products contribute additional heterogeneous interfaces, thereby enhancing the EMW absorption performance of the material [27]. To quantitatively characterize the crystal structure parameters of the $(\text{Fe}_{1-x}\text{Mn}_x)_2\text{AlB}_2$ samples, Rietveld refinement of the XRD patterns was performed using the GSAS software. As shown in Fig. S2 and Table S2, the refinement parameters yield reliability factors R_p and R_{wp} ranging from 2.89%–6.30% and 3.65%–9.80%, respectively. Collectively, these results validate the efficacy of ultrafast Joule heating-driven synthesis method in producing $(\text{Fe}_{1-x}\text{Mn}_x)_2\text{AlB}_2$ materials.

The surface electronic states of $(\text{Fe}_{1-x}\text{Mn}_x)_2\text{AlB}_2$ were systematically investigated using XPS. As clearly shown in Fig. 2(b), the XPS survey spectrum of the pristine Fe_2AlB_2 ($x = 0$) confirms the coexistence of five elements: Fe, O, C, B, and Al. Progressive Mn substitution induces notable spectral evolution. At $x = 0.7$, characteristic Mn 2p peaks emerge while residual Fe 2p signals persist alongside other constituent elements. Fully substitution ($x = 1$, Mn_2AlB_2) results in the complete disappearance of Fe 2p features, yielding a spectrum dominated exclusively by Mn, O, C, B, and Al

components. This systematic evolution provides direct evidence for full compositional transition from Fe- to Mn-based MAB phases through substitutional doping. To further elucidate the chemical states, Figs. 2(c)–(f) present the high-resolution XPS spectra of Fe 2p, Mn 2p, Al 2p, and B 1s for the representative $(\text{Fe}_{0.3}\text{Mn}_{0.7})_2\text{AlB}_2$ sample. The Fe 2p spectrum exhibits characteristic peaks at 706.41 eV and 719.1 eV, corresponding to Fe 2p_{3/2} and Fe 2p_{1/2}, respectively. The Mn 2p spectrum displays complexity with three distinct oxidation states: The primary peaks at 640.8 eV and 652.1 eV are assigned to Mn^{2+} 2p_{3/2} and Mn^{2+} 2p_{1/2}, respectively, whereas those at 642.3/652.9 eV and 643.2/654.2 eV are attributed to Mn^{3+} and Mn^{4+} species, respectively. The observed coexistence of Mn^{2+} , Mn^{3+} , and Mn^{4+} oxidation states likely originates from minor surface oxidation [27–29]. Additionally, the Al 2p (74.10 eV) and B 1s (187.95 eV) binding energies align well with reported values for MAB phase compounds. Combined with comparative XPS data for Fe_2AlB_2 and Mn_2AlB_2 (Figs. S3 and S4), these results validate the successful synthesis of $(\text{Fe}_{1-x}\text{Mn}_x)_2\text{AlB}_2$ solid solutions across the entire composition range.

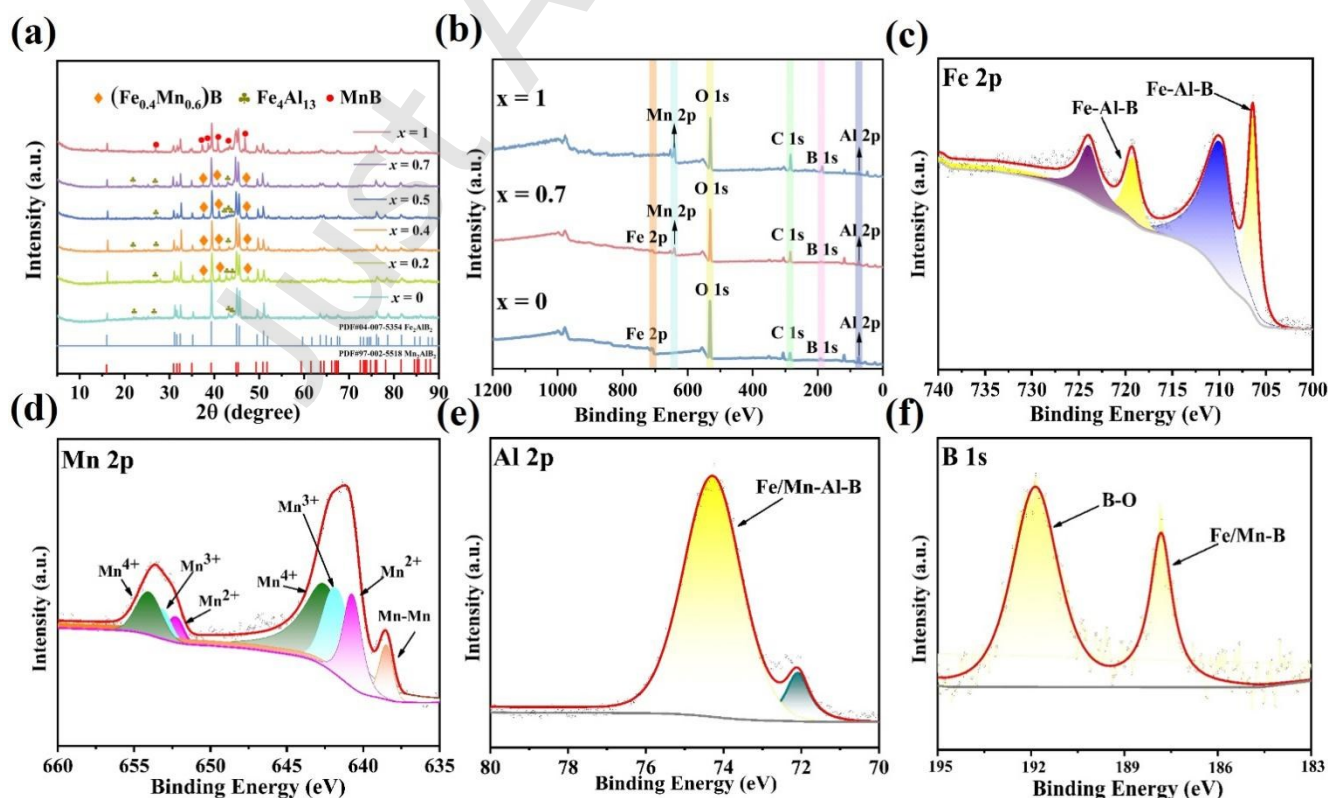


Fig. 2 (a) XRD patterns of the $(\text{Fe}_{1-x}\text{Mn}_x)_2\text{AlB}_2$ samples ($x = 0, 0.2, 0.4, 0.5, 0.7, \text{ and } 1$). (b) Survey XPS spectrum of the $(\text{Fe}_{1-x}\text{Mn}_x)_2\text{AlB}_2$ samples ($x = 0, 0.7, \text{ and } 1$). High-resolution (c) Fe 2p, (d) Mn 2p, (e) Al 2p, and (f) B 1s XPS spectra of the $(\text{Fe}_{0.3}\text{Mn}_{0.7})_2\text{AlB}_2$ sample.

Figs. 3(a) and (b) show the SEM images of the $(\text{Fe}_{0.3}\text{Mn}_{0.7})_2\text{AlB}_2$ sample, which reveal a clear laminar structure and the presence of grains. The particle size distribution of the $(\text{Fe}_{0.3}\text{Mn}_{0.7})_2\text{AlB}_2$ sample shown in Fig. S5 is approximately normal, with an average particle size (D_{50}) of 9.537 μm and a D_{90} (D_{90} is defined such that 90% of the particles have a diameter smaller than or equal to this value) of 23.328 μm . For comparison, the average particle size of Fe_2AlB_2 prepared using the combustion synthesis hot pressing method in a previous work was reported to be 12.8 μm , with a maximum particle size of 57 μm [30]. This result confirms that the grain size can be effectively refined through Joule heating-driven ultrafast synthesis. Within MAB phase systems, reduced particle dimensions yield increased specific surface areas that amplify EMW-material interactions via multiscale scattering phenomena and energy dissipation mechanisms. Crucially, the reduced-dimension particles intensify interfacial polarization effects, enabling efficient electromagnetic energy conversion through thermal dissipation processes. Fig. 3(c) presents the high-angle annular dark-field scanning transmission electron microscopy (HAADF-STEM) images and corresponding EDS elemental mapping images, which show a uniform distribution of the Fe, Mn, Al, and B elements. Fig. 3(d) shows a high-resolution transmission electron microscopy (HRTEM) image, which clearly displays lattice fringes with a spacing of 0.229 nm (calculated by averaging the total distance across 20 planes), which corresponds to the (130) crystal planes of $(\text{Fe}_{0.3}\text{Mn}_{0.7})_2\text{AlB}_2$. Fig. 3(e) exhibits discontinuous lattice fringes, indicating the presence of lattice deficiency within the grain. These structural defects are primarily attributed to the ultrafast joule-heating process, which kinetically suppresses surface diffusion-mediated defect healing. The truncated thermal exposure (<12 s dwell time) prevents atomic rearrangement required for vacancy annihilation, thereby enabling retention of vacancy clusters and dislocation networks within the consolidated

microstructure [31-32]. Fig. 3(f) shows the selected area electron diffraction (SAED) pattern of $(\text{Fe}_{0.3}\text{Mn}_{0.7})_2\text{AlB}_2$. The observed diffraction spots corresponding to the (-200) , $(01-1)$, and $(0-22)$ planes are in good agreement with the XRD data presented in Fig. 2(a). The inverse Fast Fourier Transform (IFFT)-filtered images (Figs. 3(g) and (h)) reveal the existence of lattice distortions. The emergence of these distortions is attributed to the difference in atomic radius between Mn and Fe, which can lead to local lattice expansion and consequent lattice distortions [33]. Additionally, Mn doping modifies the chemical bonding in Fe_2AlB_2 , resulting in stronger coordination bonds between Mn and B. This change in coordination also contributes to the emergence of local lattice distortions. These lattice distortions promote the formation of defects [34]. As a result, defects and lattice distortions are generated within the material through a combination of Joule heating-driven ultrafast sintering and defect engineering. The presence of these defects and lattice distortions is expected to enhance the dielectric properties of the materials and improve their microwave absorption [35-41].

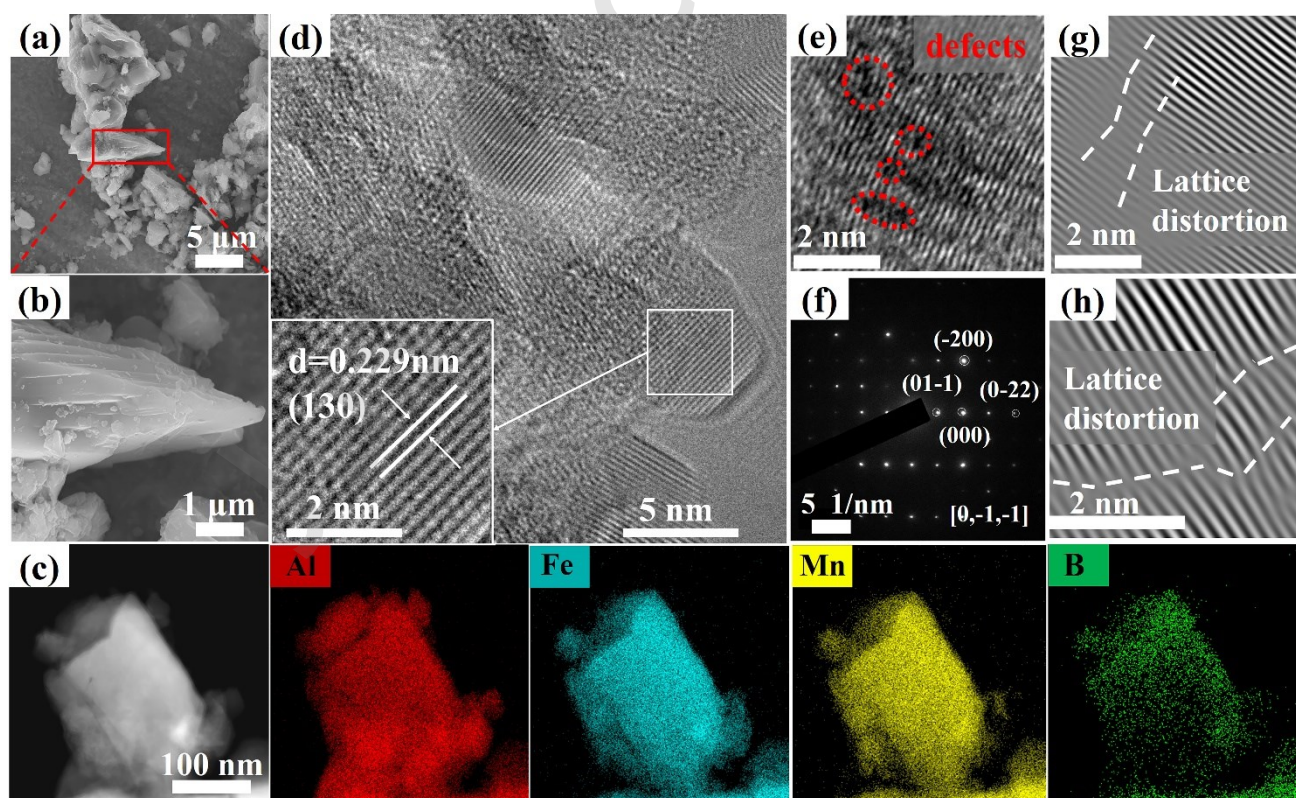


Fig. 3 (a), (b) SEM images of $(\text{Fe}_{0.3}\text{Mn}_{0.7})_2\text{AlB}_2$. (c) HAADF-STEM image and corresponding Al, Mn, Fe, and B elemental mapping images of $(\text{Fe}_{0.3}\text{Mn}_{0.7})_2\text{AlB}_2$. (d), (e) HRTEM image of

(Fe_{0.3}Mn_{0.7})₂AlB₂ and (f) SAED pattern of (Fe_{0.3}Mn_{0.7})₂AlB₂ along the [0, -1, -1] zone axis. (g), (h)

Atomic IFFT-filtered images of (Fe_{0.3}Mn_{0.7})₂AlB₂ derived from the SAED pattern.

3.2 EMW absorption properties

The absorption characteristics of the (Fe_{1-x}Mn_x)₂AlB₂ samples were evaluated by calculating their reflection loss (*RL*), which is a crucial parameter. *RL* is calculated as follows [12]:

$$RL \text{ (dB)} = 20 \log \frac{Z_{in} - Z_0}{Z_{in} + Z_0}, \quad (1)$$

$$Z_{in} = Z_0 \sqrt{\frac{\mu_r}{\epsilon_r}} \tanh \left[\left(\frac{2\pi j f d}{c} \right) \sqrt{\mu_r \epsilon_r} \right], \quad (2)$$

where Z_{in} is the impedance of the absorbing material, Z_0 is the characteristic impedance of the medium in which the wave propagates, f is the incoming microwave frequency, d is the thickness of the absorbing material, and c is the speed of light.

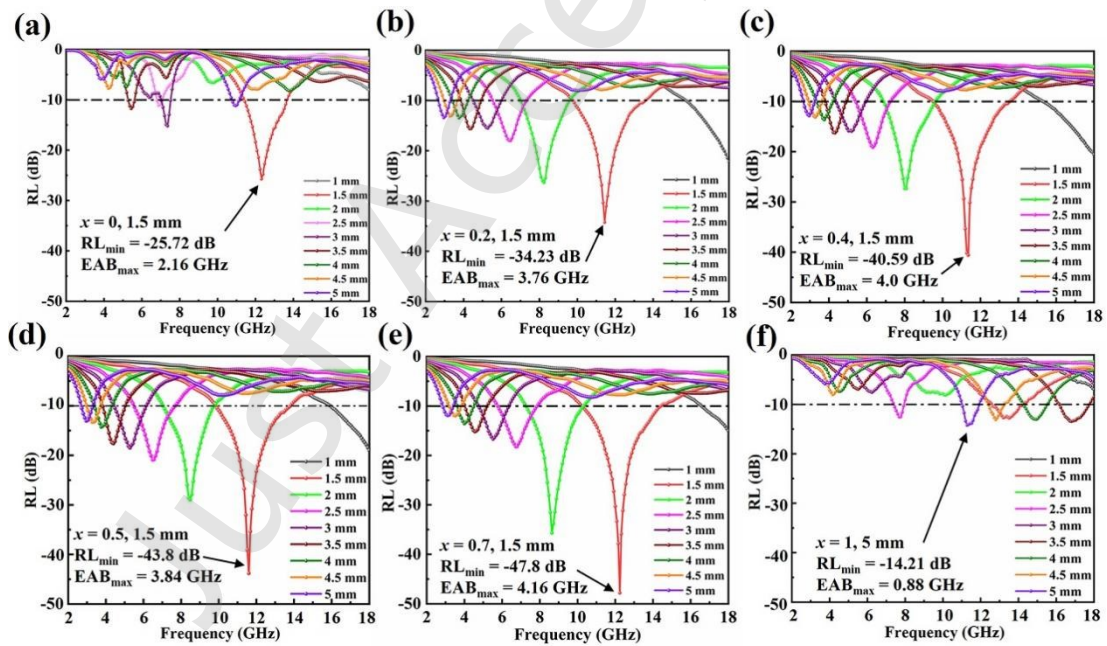


Fig. 4 RL curves of (a) Fe₂AlB₂, (b) (Fe_{0.8}Mn_{0.2})₂AlB₂, (c) (Fe_{0.6}Mn_{0.4})₂AlB₂, (d) (Fe_{0.5}Mn_{0.5})₂AlB₂, (e) (Fe_{0.3}Mn_{0.7})₂AlB₂, and (f) Mn₂AlB₂ with different thicknesses.

In general, the *RL* value is employed to assess the absorbing performance of a material. The EMW absorption performance of the (Fe_{1-x}Mn_x)₂AlB₂ samples ($x = 0, 0.2, 0.4, 0.5, 0.7$, and 1) was evaluated using a VNA. Figs. 4 and 5 depict the *RL* curves and two-dimensional (2D) *RL* contour

maps of all samples with various thicknesses in the frequency range of 2–18 GHz. As illustrated in Figs. 4(a)–(f), the $(\text{Fe}_{1-x}\text{Mn}_x)_2\text{AlB}_2$ samples with $x = 0.2-0.7$ exhibit excellent wave-absorption properties, achieving RL_{\min} values of -34.23 , -40.59 , -43.8 , and -47.8 dB, respectively, at a thickness of 1.5 mm. By contrast, the RL_{\min} values of the samples with $x = 0$ and 1 are -25.72 and -14.21 dB, respectively, at thicknesses of 1.5 and 5 mm, respectively. Thus, the RL_{\min} of these samples initially increases with increasing x , reaching a peak of -47.8 dB at $x = 0.7$, and then decreases. As shown in Figs. 5(a)–(f), the EAB_{\max} of the $(\text{Fe}_{1-x}\text{Mn}_x)_2\text{AlB}_2$ samples with $x = 0.2-0.7$ is significantly greater than that of the $(\text{Fe}_{1-x}\text{Mn}_x)_2\text{AlB}_2$ samples with $x = 0$ and 1. The maximum EAB_{\max} (4.16 GHz) is reached at $x = 0.7$. These results indicate that the samples doped with Mn exhibit a greater EMW attenuation capacity compared with the undoped sample and the sample where Mn has fully replaced Fe. Specifically, the sample with $x = 0.7$ possesses the strongest EMW attenuation capacity, and these outstanding wave-absorption characteristics will be discussed in detail later. These findings imply that introducing defects through doping is an effective strategy to enhance the EMW absorption capacity of materials. In addition, as shown in Fig. 5(g) and Table S3, $(\text{Fe}_{0.3}\text{Mn}_{0.7})_2\text{AlB}_2$ exhibits more excellent EMW absorption properties than most of the previously reported transition metal-layered compounds, proving that $(\text{Fe}_{0.3}\text{Mn}_{0.7})_2\text{AlB}_2$ is promising as a highly efficient and lightweight EMW absorber for practical applications.

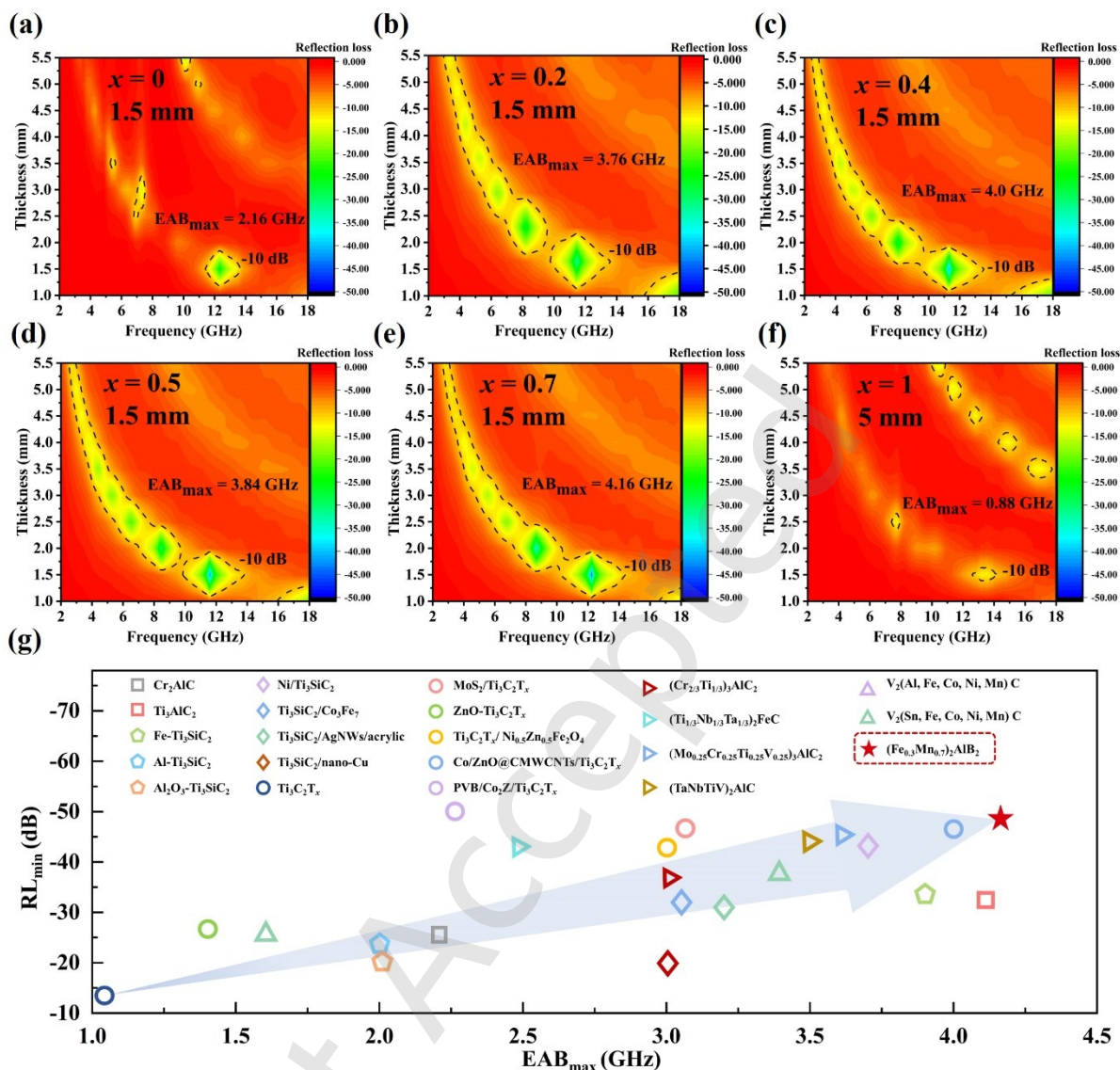


Fig. 5 2D RL contour maps of (a) Fe_2AlB_2 , (b) $(\text{Fe}_{0.8}\text{Mn}_{0.2})_2\text{AlB}_2$, (c) $(\text{Fe}_{0.6}\text{Mn}_{0.4})_2\text{AlB}_2$, (d) $(\text{Fe}_{0.5}\text{Mn}_{0.5})_2\text{AlB}_2$, (e) $(\text{Fe}_{0.3}\text{Mn}_{0.7})_2\text{AlB}_2$, and (f) Mn_2AlB_2 . (g) EMW absorption performance of $(\text{Fe}_{0.3}\text{Mn}_{0.7})_2\text{AlB}_2$ versus other transition metal-layered compound absorbers in previous reports.

3.3 EMW absorption mechanism and EM parameters of the $(\text{Fe}_{1-x}\text{Mn}_x)_2\text{AlB}_2$ samples

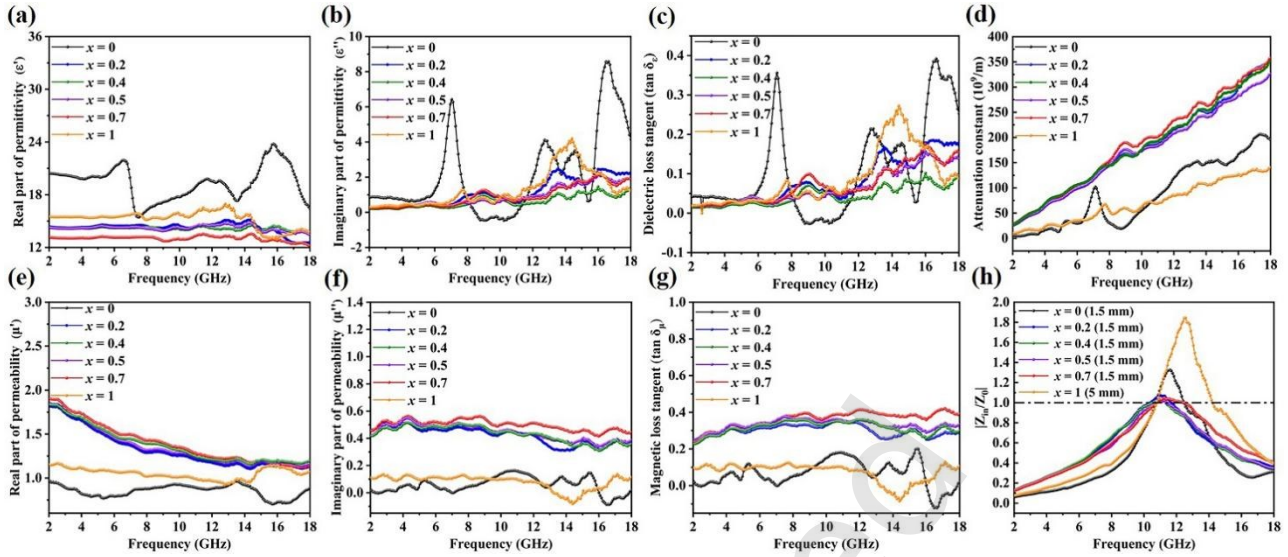


Fig. 6 EMW absorption properties of the $(\text{Fe}_{1-x}\text{Mn}_x)_2\text{AlB}_2$ samples ($x = 0, 0.2, 0.4, 0.5, 0.7$, and 1): (a) real part of the complex permittivity ϵ' , (b) imaginary part of the complex permittivity ϵ'' , (c) dielectric loss tangent $\tan \delta_\epsilon$, (d) attenuation constant α , (e) real part of the complex permeability μ' , (f) imaginary part of the complex permeability μ'' , (g) magnetic loss tangent $\tan \delta_\mu$, and (h) Z_{in}/Z_0 .

A comprehensive investigation of the dielectric constant ($\epsilon_r = \epsilon' - j\epsilon''$) and magnetic permeability ($\mu_r = \mu' - j\mu''$) in the 2–18 GHz frequency band is necessary to gain a deeper understanding of the microwave absorption mechanism of the $(\text{Fe}_{1-x}\text{Mn}_x)_2\text{AlB}_2$ samples. The EM energy storage capacity is represented by the real parts (ϵ' and μ'), whereas the ability to dissipate EM energy is represented by the imaginary parts (ϵ'' and μ''). Fig. 6(a) illustrates that ϵ' exhibits a comparable fluctuating trend in the high-frequency range (10–18 GHz) for all samples, except for the undoped sample. This is attributed to the orientation of the polarization of the intrinsic electric dipoles and the polarization of the space charges in the high-frequency range (10–18 GHz) [42]. The undoped sample shows maxima in ϵ' at 6.9, 11.8, and 16.0 GHz and a decrease in ϵ' at higher frequencies. This can be attributed to the polarization lag that occurs under the influence of an electric field [27]. The multiple fluctuations observed for ϵ'' are attributed to the dipole and interfacial polarizations (Fig. 6(b)). This polarization complexity originates from Mn-induced lattice distortions at M-sites coupled with defect generation during Joule-driven thermal cycling - a dual structural modification conclusively

demonstrated through atomic IFFT-filtered and HRTEM images (Fig. 3). These defects and lattice distortions act as polarization centers, hindering the reorientation of dipoles and the rearrangement of space charges under an alternating electric field. This results in energy dissipation, thereby increasing the dielectric loss of the material. The increase in dielectric loss is usually manifested as an increase in the imaginary part of the permittivity (ϵ'') [42]. The fluctuations in ϵ'' and dielectric loss tangent ($\tan \delta_\epsilon = \epsilon''/\epsilon'$) illustrated in Figs. 6(b) and (c) are comparable for the various samples, with multiple relaxation peaks within the 6–18 GHz range, indicating the possible occurrence of polarization relaxation phenomena [27].

The attenuation constant (α) is another important parameter for assessing the performance of EMW absorbers. It is calculated as follows [43]:

$$\alpha = \left(\frac{\sqrt{2}\pi f}{c} \right) \times \sqrt{(u''\epsilon'' - u'\epsilon') + \sqrt{(u''\epsilon'' - u'\epsilon') + (u''\epsilon' + u'\epsilon'')^2}}. \quad (3)$$

The attenuation constant of the $(\text{Fe}_{1-x}\text{Mn}_x)_2\text{AlB}_2$ samples with $x = 0.2-0.7$ is typically larger than that of the $(\text{Fe}_{1-x}\text{Mn}_x)_2\text{AlB}_2$ samples with $x = 0$ and 1, with the highest attenuation constant observed at $x = 0.7$. This indicates that $(\text{Fe}_{0.3}\text{Mn}_{0.7})_2\text{AlB}_2$ exhibits exceptional EMW attenuation properties, as illustrated in Fig. 6(d). Additionally, this finding suggests that Mn incorporation at the M site of Fe_2AlB_2 is an effective method for enhancing its EMW attenuation capability.

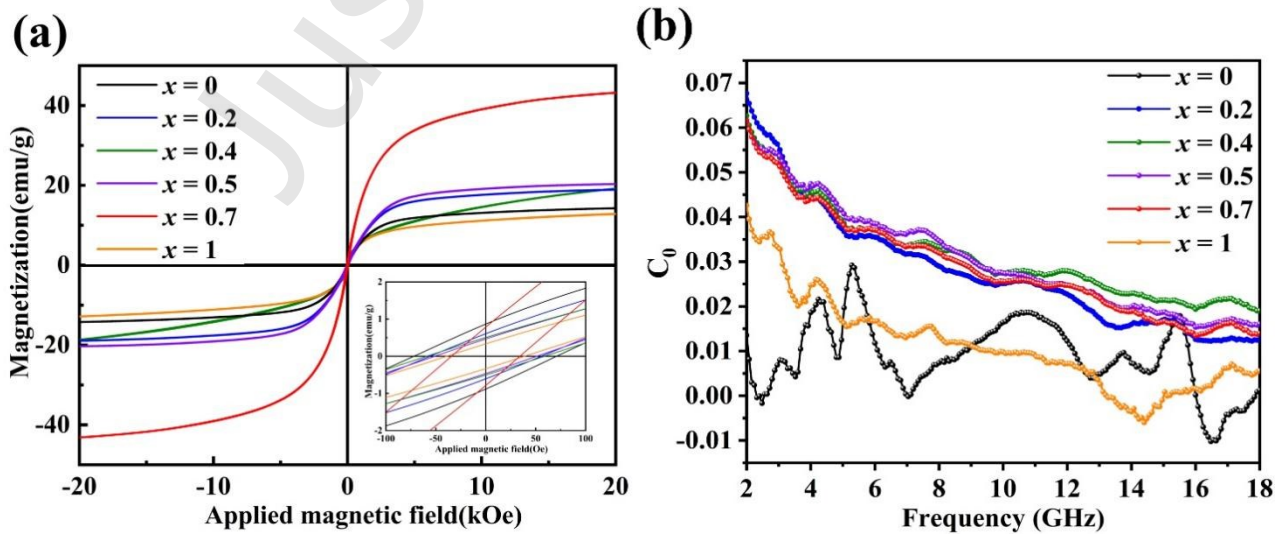


Fig. 7 (a) Hysteresis loops, (b) C_0 curves of the $(\text{Fe}_{1-x}\text{Mn}_x)_2\text{AlB}_2$ samples. The inset in panel (a) shows a magnified view of the loops in the magnetic field range from -100 to 100 Oe.

Fig. 6(e) illustrates that the overall μ' of the $(\text{Fe}_{1-x}\text{Mn}_x)_2\text{AlB}_2$ samples with $x = 0.2-0.7$ is reduced with increasing frequency. This can be attributed to the intrinsic magnetic resonance occurring in these samples. The μ' of the $(\text{Fe}_{1-x}\text{Mn}_x)_2\text{AlB}_2$ samples with $x = 0$ and 1 is lower than that of the other samples, which is due to the fact that the low saturation magnetization (M_S) of these two samples decreases their μ' value (Fig. 7(a)) [44]. Furthermore, μ'' is usually used to evaluate the magnetic loss capability of a material. The μ'' of the $(\text{Fe}_{1-x}\text{Mn}_x)_2\text{AlB}_2$ samples exhibits an initial increase with increasing x , reaching the maximum at $x = 0.7$ and subsequently decreasing (Fig. 6(f)). This suggests that Mn doping enhances the magnetic loss capability of the $(\text{Fe}_{1-x}\text{Mn}_x)_2\text{AlB}_2$ samples. The magnetic loss tangent ($\tan \delta_\mu = \mu''/\mu'$) has a similar trend as a function of x as that of μ'' . As illustrated in Fig. 6(g), the greatest magnetic loss tangent loss is observed at $x = 0.7$. The magnetic loss contribution has a more pronounced impact on the overall EMW loss capacity of the $(\text{Fe}_{1-x}\text{Mn}_x)_2\text{AlB}_2$ samples compared with the dielectric loss contribution. Magnetic losses mainly stem from domain wall resonance, hysteresis, eddy current loss, natural resonance, and exchange resonance. The domain wall resonance loss usually occurs at low frequencies (MHz) [45]. In addition, the eddy current loss can be estimated as follows [46]:

$$C_0 = u''(u')^{-2}f^{-1} = \frac{(2\pi u_0 \sigma D^2)}{3}, \quad (4)$$

where σ represents the electrical conductivity of the material, D is the matching thickness, and μ_0 denotes the vacuum permeability. Magnetic losses are only caused by eddy current losses if C_0 is constant; otherwise, they are caused by exchange resonance or natural resonance [47]. As illustrated in Fig. 7(b), the curves of the C_0 values of the six samples as a function of frequency unambiguously demonstrate that magnetic resonance is the predominant source of the magnetic losses in the $(\text{Fe}_{1-x}\text{Mn}_x)_2\text{AlB}_2$ samples. Concerning the magnetic resonance mechanism, the complex permeability

spectra ($\mu''-f$) of all samples can be fitted with the Landau–Lifshitz–Gilbert (LLG) equation [48], and the relationship is expressed as follows:

$$\mu'' = \sum_i^n x_i' \frac{\left(\frac{f}{f_i}\right)\beta \left[1 + \left(\frac{f}{f_i}\right)^2 (1 + \beta^2)\right]}{\left[1 - \left(\frac{f}{f_i}\right)^2 (1 + \beta^2)\right]^2 + 4\beta^2 \left(\frac{f}{f_i}\right)^2}, \quad (5)$$

where n is the number of μ'' peaks, x_i' is the initial magnetization, f_i is the natural resonance frequency, and β is the damping factor. To understand the effect of hysteresis loss on the $(\text{Fe}_{1-x}\text{Mn}_x)_2\text{AlB}_2$ samples, their hysteresis return line was investigated, as shown in Fig. 7(a). The saturation magnetization and coercivity can be extracted from the hysteresis loops, and the corresponding values are provided in Table S4. As x increases, M_s also increases, reaching a maximum value of 43.2 emu/g at $x = 0.7$. Concurrently, the coercivity (H_c) declines and reaches a minimum value of 32.1 Oe at $x = 0.7$. The anomalous behavior of the sample with $x = 0.7$ can be attributed to the occurrence of a super-magnetic jump, as previously demonstrated by Shiotani et al. [14]. In this jump, the saturation magnetization of the material grows dramatically as the applied magnetic field increases [49]. This is due to the applied magnetic field disrupting the initial antiferromagnetic order, leading to a progressive tendency of the magnetic moments to align parallel to each other and a consequent increase in the saturation magnetization of the material. $(\text{Fe}_{0.3}\text{Mn}_{0.7})_2\text{AlB}_2$ is readily magnetized and exhibits a rapid response to external electromagnetic fields, owing to its high saturation magnetization and low coercivity. This increases the energy consumption during the rotation of the magnetic domains [42]. In conclusion, magnetic resonance and hysteresis loss are the two primary magnetic loss mechanisms in the investigated samples. Both processes are capable of efficiently dissipating EM energy. In addition, optimized impedance matching ($Z = |Z_{in}/Z_0|$) results in a high EMW absorption performance [50-51]. A Z value of 1 indicates that the impedance matching of the material is optimal, which facilitates the penetration of EMW into the material and their effective absorption [52]. As can be seen from Fig. 6(h), for the $(\text{Fe}_{1-x}\text{Mn}_x)_2\text{AlB}_2$ samples with $x = 0.2-0.7$, the thickness at which RL is minimum corresponds to a Z

value close to 1. The $(\text{Fe}_{1-x}\text{Mn}_x)_2\text{AlB}_2$ samples exhibit improved impedance matching, demonstrating that Mn doping plays a key role in modulating the impedance matching properties of Fe_2AlB_2 . Specifically, it is clear that over a broader frequency range, the Z value of $(\text{Fe}_{0.3}\text{Mn}_{0.7})_2\text{AlB}_2$ approaches 1. This indicates that the excellent impedance matching of $(\text{Fe}_{0.3}\text{Mn}_{0.7})_2\text{AlB}_2$ contributes to the outstanding EMW absorption performance of this sample.

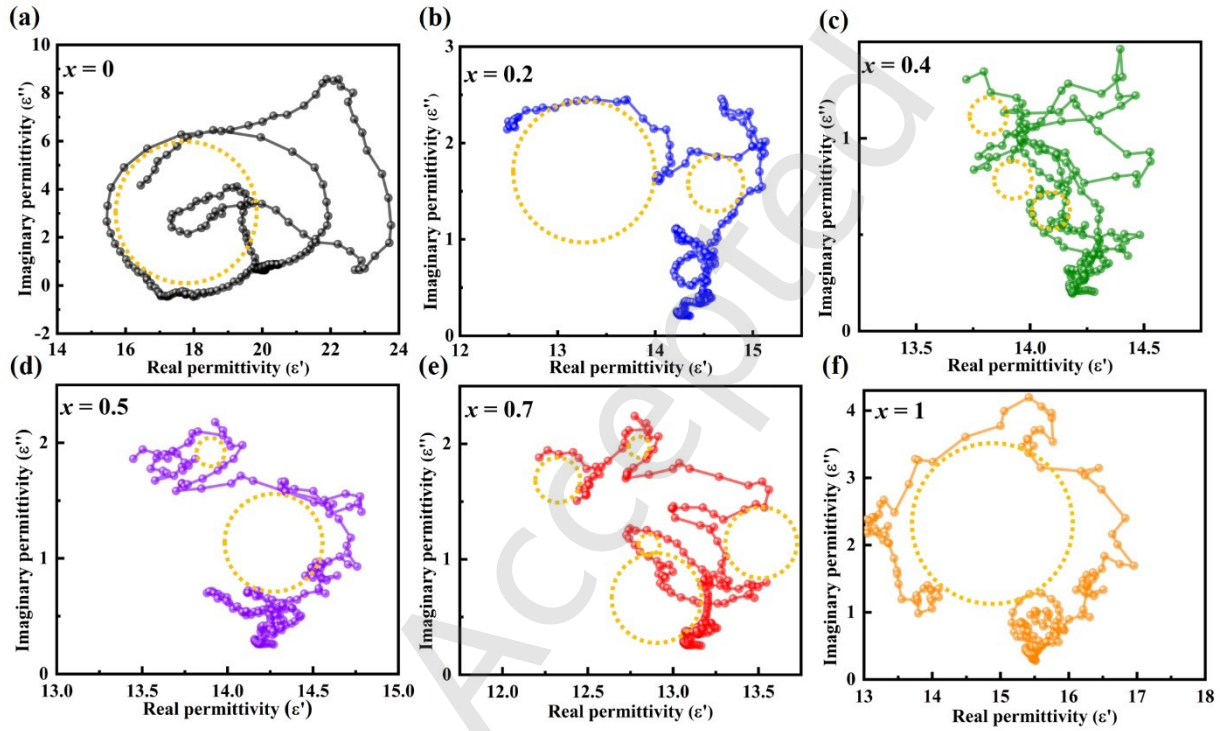


Fig. 8 Cole–Cole diagrams of the $(\text{Fe}_{1-x}\text{Mn}_x)_2\text{AlB}_2$ samples with (a) $x = 0$, (b) $x = 0.2$, (c) $x = 0.4$, (d) $x = 0.5$, (e) $x = 0.7$, and (f) $x = 1$.

The dipole polarization relaxation can be explained by the Debye relaxation theory, and the relationship between ϵ' and ϵ'' can be expressed as follows [53]:

$$\left[\epsilon' - \frac{(\epsilon_s + \epsilon_\infty)}{2} \right]^2 + (\epsilon'')^2 = \left[\frac{\epsilon_s - \epsilon_\infty}{2} \right]^2, \quad (6)$$

where ϵ_∞ and ϵ_s represent the dielectric constant at infinite frequency and the static dielectric constant, respectively. If ϵ' and ϵ'' satisfy the condition set out in Eq. (6), the ϵ'' – ϵ' curve will form a semicircle, which is known as the Cole–Cole semicircle. This behavior, as illustrated in Figs. 8(a) and (f), occurs when the polarization loss is solely due to dipole polarization relaxation. Each semicircle

corresponds to a Debye dipole relaxation process. As mentioned above, polarization relaxation loss leads to dielectric loss, which manifests itself with fluctuations in the $\tan \delta_\epsilon$ curve (Fig. 6(c)) in the frequency range of 2–18 GHz as well as the Cole–Cole diagrams in Fig. 8. As depicted in Fig. 8, the ϵ'' – ϵ' curves demonstrate multiple distinct Cole-Cole semicircles, where an increased semicircle multiplicity correlates with enhanced polarization relaxation processes within the absorber. In Figs. 8(a) and (f), the limited semicircle multiplicity reflects restricted polarization mechanisms, which can be attributed to constrained polarization mechanisms. In contrast, Figs. 8(b-e) display multiple distorted and non-standard semicircles, indicative of simultaneous activation of dipole polarization and interfacial polarization under alternating electromagnetic fields [45]. This phenomenon primarily stems from doping-induced structural modifications. Mn/Fe substitution significantly increases heterogeneous interfaces, thereby amplifying interfacial polarization. When irradiated by EMW, interfacial charge accumulation occurs both at stacked interlayer boundaries and phase interfaces (e.g., between $(\text{Fe}_{1-x}\text{Mn}_x)_2\text{AlB}_2$ matrix and secondary phases), inducing interfacial polarization relaxation [13]. Concurrently, the doping process introduces lattice distortion defects and vacancy clusters, which function as dipole polarization centers. These defect-induced dipoles exhibit enhanced oscillation synchronization with incident EMW, substantially improving dipole polarization efficiency.

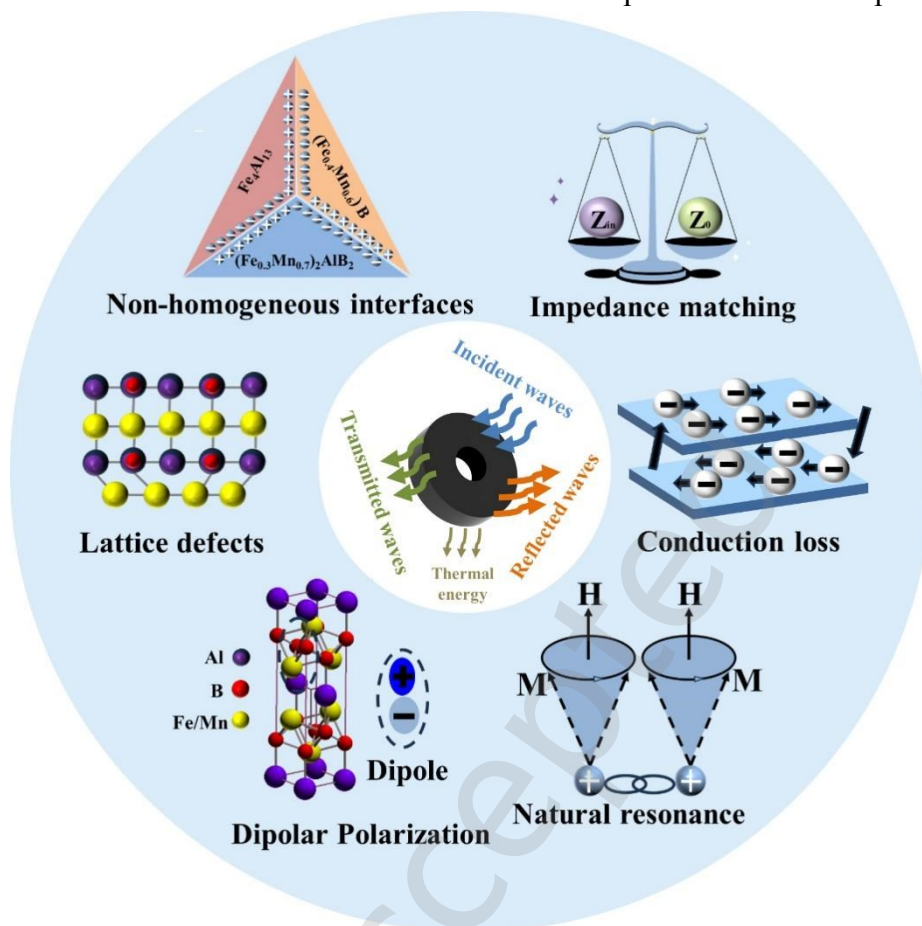


Fig. 9. Microwave absorption mechanisms of $(\text{Fe}_{0.3}\text{Mn}_{0.7})_2\text{AlB}_2$.

The mechanisms of EMW absorption are illustrated in Fig. 9 taking the $(\text{Fe}_{0.3}\text{Mn}_{0.7})_2\text{AlB}_2$ sample as an example. Being a conventional MAB phase, $(\text{Fe}_{0.3}\text{Mn}_{0.7})_2\text{AlB}_2$ exhibits good electrical conductivity due to the strong metallic bonding within the M layer. Consequently, it can provide conduction losses by generating heat and dissipating EMW. Furthermore, Mn is incorporated at the M site of $(\text{Fe}_{0.3}\text{Mn}_{0.7})_2\text{AlB}_2$, where it replaces Fe, resulting in an uneven charge distribution. This uneven charge distribution leads to dipole enrichment and promotes the relaxation process of the dipole polarization. In addition, non-homogeneous interfaces with different charge distributions form between $(\text{Fe}_{0.3}\text{Mn}_{0.7})_2\text{AlB}_2$ and the various constituent phases, namely $\text{Fe}_4\text{Al}_{13}$ and $(\text{Fe}_{0.4}\text{Mn}_{0.6})\text{B}$. These interfaces give rise to multiple interfacial polarization relaxation processes, thereby enhancing EMW attenuation. Doping with Mn, combined with the rapid sintering and cooling processes, leads to the formation of defects and lattice distortions. Consequently, the free electrons in

(Fe_{0.3}Mn_{0.7})₂AlB₂, when subjected to an external electric field, accumulate at these defects and lattice distortions, resulting in space charge polarization. Finally, magnetic resonance loss and hysteresis loss are dominant contributions to the magnetic loss of (Fe_{0.3}Mn_{0.7})₂AlB₂. (Fe_{0.3}Mn_{0.7})₂AlB₂ exhibits a high saturation magnetization and a low coercivity, which results in a rapid response to external EM fields and increases energy dissipation during the rotation of the magnetic domains. Therefore, Mn doping combined with Joule heating-driven ultrafast synthesis not only enhances conduction loss, polarization loss, magnetic resonance loss, and hysteresis loss but also promotes the formation of defects. As a result of these synergistic effects, both the dielectric and magnetic losses of the (Fe_{1-x}Mn_x)₂AlB₂ samples are increased, leading to an outstanding EMW absorption performance.

4 Conclusion

In conclusion, we successfully synthesized (Fe_{1-x}Mn_x)₂AlB₂ samples ($x = 0, 0.2, 0.4, 0.5, 0.7$, and 1) using Joule heating-driven ultrafast synthesis, resulting in improved EMW absorption performance. Mn doping enhanced dielectric loss through defects and lattice distortions, leading to stronger EMW attenuation for samples with $x = 0.2-0.7$. Notably, due to the occurrence of a super-magnetic jump in (Fe_{0.3}Mn_{0.7})₂AlB₂, the saturation magnetization and magnetic loss of the material are enhanced. As a result, (Fe_{0.3}Mn_{0.7})₂AlB₂ exhibits exceptional EMW absorption, with an EAB_{max} of 4.16 GHz and an RL_{min} of -47.8 dB at an ultralow thickness of 1.5 mm. This work demonstrates an innovative approach for synthesizing MAB phases and establishes a defect engineering framework to enhance their EMW absorption performance. Future studies should harness this integrated methodology to explore advanced MAB phase while precisely tuning defect configurations. These synergistic efforts could propel the development of MAB materials with programmable electromagnetic functionalities for emerging applications.

Availability of data and materials

The data that support the findings of this study are available from the corresponding author upon reasonable request.

Competing interests

The authors have no competing interests to declare that are relevant to the content of this article.

Funding

This work was financially supported by the National Natural Science Foundation of China (Grant Nos. 52202069, 52402089 and 52102144) and Young Talent Fund of Xi'an Association for Science and Technology (Grant Nos. 959202313074).

Author contributions

Yuhang Bai: Methodology, Investigation, Data Curation, Writing - Review & Editing. **Zelong Yao:** Investigation, Formal analysis, Writing - Original Draft. **Yang Yang:** Data curation, Investigation. **Jinrui Li:** Investigation. **Jia Liu:** Methodology. **Peipei Wang:** Methodology. **Huiling Du:** Project administration. **Xing Zhao:** Formal analysis, Project administration, Supervision. **Laifei Cheng:** Funding acquisition, Project administration, Resources, Writing - review & editing.

Acknowledgements

Thanks to eceshi (www.eceshi.com) for the XRD and XPS analysis.

Electronic Supplementary Material (ESM)

Supplementary material is available in the online version of this article.

References

- [1] Cao Q, Zhang J, Zhang H, *et al.* Dual-surfactant templated hydrothermal synthesis of CoSe₂ hierarchical microclews for dielectric microwave absorption. *J Adv Ceram.* 2022, 11: 504-514.
- [2] Hu F, Zhang F, Wang X, *et al.* Ultrabroad band microwave absorption from hierarchical MoO₃/TiO₂/Mo₂TiC₂Tx hybrids via annealing treatment. *J Adv Ceram.* 2022, 11: 1466-1478.
- [3] Niu H, Jiang X, Xia Y, *et al.* Construction of hydrangea-like core-shell SiO₂@Ti₃C₂Tx@CoNi microspheres for tunable electromagnetic wave absorbers. *J Adv Ceram.* 2023, 12: 711-723.
- [4] Wang S, Liu Q, Li S, *et al.* Joule-Heating-Driven Synthesis of a Honeycomb-Like Porous Carbon Nanofiber/High Entropy Alloy Composite as an Ultralightweight Electromagnetic Wave Absorber. *ACS Nano* 2024, 18: 5040-5050.
- [5] Wang Z, Zhang F, Wang N, *et al.* Ternary layered boride MoAlB: A novel thermo-regulation microwave absorbing ceramic material. *J Adv Ceram.* 2024, 13: 699-710.
- [6] Wu C, Zhang F, Zhi Q, *et al.* From binary to ternary and back to binary: Transition of electromagnetic wave shielding to absorption among MAB phase Ni₃ZnB₂ and corresponding binary borides Ni_{n+1}B_n (n = 1, 3). *J Adv Ceram.* 2023, 12: 2101-2111.
- [7] Kota S, Sokol M, Barsoum M W. A progress report on the MAB phases: atomically laminated, ternary transition metal borides. *Int. Mater. Rev.* 2020, 65: 226-255.
- [8] Li N, Bai Y, Wang S, *et al.* Rapid synthesis, electrical, and mechanical properties of polycrystalline Fe₂AlB₂ bulk from elemental powders. *J. Am. Ceram. Soc.* 2017, 100: 4407-4411.
- [9] Cedervall J, Andersson M S, Sarkar T, *et al.* Magnetic structure of the magnetocaloric compound AlFe₂B₂. *J. Alloys Compd.* 2016, 664: 784-791.
- [10] Levin E M, Jensen B A, Barua R, *et al.* Effects of Al content and annealing on the phases formation, lattice parameters, and magnetization of Al_xFe₂B₂(x=1.0,1.1,1.2) alloys. *Phys. Rev. Mater.* 2018, 2: 034403.
- [11] Luo W, Liu Y, Wang C, *et al.* Molten salt assisted synthesis and electromagnetic wave

absorption properties of $(V_{1-x-y}Ti_xCr_y)_2AlC$ solid solutions. *J. Mater. Chem. C*. 2021, 9: 7697-7705.

[12] Li J, Xu T, Bai H, *et al.* Structural Modifications and Electromagnetic Property Regulations of Ti_3AlC_2 MAX for Enhancing Microwave Absorption through the Strategy of Fe Doping. *Adv. Mater. Interfaces*. 2022, 9: 2101510.

[13] Han J, Chen Q, Wang Y, *et al.* Anomalous electromagnetic wave absorption of MAX phase ceramic powder achieved through high entropy solid solution and melt pool heat transfer preparation method. *J. Mater. Sci.: Mater. Electron*. 2024, 35: 883.

[14] Shiotani T, Waki T, Tabata Y, *et al.* Competing magnetic correlations and uniaxial anisotropy in $(Fe_{1-x}Mn_x)_2AlB_2$ single crystals. *Phys. Rev. Mater*. 2024, 8: 054412.

[15] Melikhov Y, Snyder J E, Jiles D C, *et al.* Temperature dependence of magnetic anisotropy in Mn-substituted cobalt ferrite. *J. Appl. Phys*. 2006, 99: 08R102.

[16] Jia J, Liu C, Ma N, *et al.* Exchange coupling controlled ferrite with dual magnetic resonance and broad frequency bandwidth in microwave absorption. *Sci. Technol. Adv. Mat*. 2013, 14: 045002.

[17] Wang C, Ping W, Bai Q, *et al.* A general method to synthesize and sinter bulk ceramics in seconds. *Science* 2020, 368: 521-526.

[18] Ramasamy S. Investigation of nanostructured materials by positron annihilation. *Metals Mater. Process*. 1996, 8: 61-73.

[19] Kusunoki H, Kondo T, Hiraki K, *et al.* Grain-size dependence of absorption characteristics of the electromagnetic wave absorbers of ferrite-SiO₂ composites *Electr. Eng. Jpn*. 2004, 146: 1-9.

[20] Bowen C, Open J, Fitzmaurice J, *et al.* Fast firing of electroceramics. *Ferroelectrics* 1999, 228: 159-166.

[21] Biesuz M, Spiridigliozzi L, Frasnelli M, *et al.* Rapid densification of Samarium-doped Ceria ceramic with nanometric grain size at 900-1100°C. *Mater. Lett*. 2017, 190: 17-19.

[22] Esposito V, Traversa E. Design of Electroceramics for Solid Oxides Fuel Cell Applications: Playing with Ceria. *J. Am. Ceram. Soc*. 2008, 91: 1037-1051.

- [23] Bai YH, Li J, Lu H, *et al.* Ultrafast high-temperature sintering of high-entropy oxides with refined microstructure and superior lithium-ion storage performance. *J Adv Ceram.* 2023, 12: 1857-1871.
- [24] Zhao X, Wu W, Bai Y, *et al.* Microstructure evolution and densification behavior of ultrafast high-temperature sintered $\text{Li}_{6.5}\text{La}_3\text{Zr}_{1.5}\text{Ta}_{0.5}\text{O}_{12}$ ceramics. *J Power Sources.* 2024, 613: 234913.
- [25] Liu J, Li S, Yao B, *et al.* Rapid synthesis and characterization of a nanolaminated Fe_2AlB_2 compound. *J. Alloys Compd* 2018, 766: 488-497.
- [26] Liang B, Zhu D, Zhang Q, *et al.* Preparation of Mn_2AlB_2 Material via Thermal Explosion. *Russ. J. Non-Ferrous Met.* 2022, 63: 448-455.
- [27] Zhi Q, Wu C, Li M, *et al.* Fe_2AlB_2 : A novel ferromagnetic material with superior electromagnetic wave absorption performance. *Ceram. Int.* 2023, 49: 34182-34190.
- [28] Benamor A, Hadji Y, Kota S, *et al.* Friction and wear characteristics of the nanolaminated ternary transition metal boride: Mn_2AlB_2 . *Wear* 2022, 492/493: 204232.
- [29] Natu V, Kota S S, Barsoum M W. X-ray photoelectron spectroscopy of the MAB phases, MoAlB , M_2AlB_2 ($\text{M} = \text{Cr}, \text{Fe}$), Cr_3AlB_4 and their binary monoborides. *J. Eur. Ceram. Soc.* 2020, 40: 305-314.
- [30] Potanin A Y, Bashkirov E A, Karpenkov A Y, *et al.* Fabrication of high-strength magnetocaloric Fe_2AlB_2 MAB phase ceramics via combustion synthesis and hot pressing. *Materialia* 2024, 33: 101993.
- [31] Mishra T P, Wang S, Lenser C, *et al.* Ultra-fast high-temperature sintering of strontium titanate. *Acta Materialia.* 2022, 231: 117918.
- [32] German R M. Rapid Heating Concepts in Sintering. *J. Korean Powder Metall. Inst.* 2013, 20: 85-99.
- [33] Lesturgez S, Goglio G, Duttine M, *et al.* Tuning the Mn and Fe Valence States into New $\text{Ca}_{0.7}\text{Mn}_{2-x}\text{Fe}_x\text{O}_4$ ($0 < x \leq 0.60$) Solid Solution during Reversible Redox Processes. *Chem. Mater.*

- [34] Qiu Z, Liu X, Yang T, *et al.* Synergistic Enhancement of Electromagnetic Wave Absorption and Corrosion Resistance Properties of High Entropy Alloy Through Lattice Distortion Engineering. *Adv. Funct. Mater.* 2024, 34: 2400220.
- [35] Meng B, Klein B D B, Booske J H, *et al.* Microwave absorption in insulating dielectric ionic crystals including the role of point defects. *Phys. Rev. B.* 1996, 53: 12777-12785.
- [36] Guo W, Ma Z, Luo Y, *et al.* Structure, defects, and microwave dielectric properties of Al-doped and Al/Nd co-doped $\text{Ba}_4\text{Nd}_{9.33}\text{Ti}_{18}\text{O}_{54}$ ceramics. *J. Adv. Ceram.* 2022, 11: 629-640.
- [37] Wang F, Gu W, Chen J, *et al.* The point defect and electronic structure of K doped $\text{LaCo}_{0.9}\text{Fe}_{0.1}\text{O}_3$ perovskite with enhanced microwave absorbing ability. *Nano Res.* 2021, 15: 3720-3728.
- [38] Zhang W, Xiang H, Dai F-Z, *et al.* Achieving ultra-broadband electromagnetic wave absorption in high-entropy transition metal carbides (HE TMCs). *J Adv Ceram.* 2022, 11: 545-555.
- [39] Zhang W, Zhao B, Xiang H, *et al.* One-step synthesis and electromagnetic absorption properties of high entropy rare earth hexaborides (HE REB_6) and high entropy rare earth hexaborides/borates (HE $\text{REB}_6/\text{HE REBO}_3$) composite powders. *J Adv Ceram.* 2021, 10: 62-77.
- [40] Xiang H, Xing Y, Dai F-z, *et al.* High-entropy ceramics: Present status, challenges, and a look forward. *J Adv Ceram.* 2021, 10: 385-441.
- [41] Ma J, Zhao B, Xiang H, *et al.* High-entropy spinel ferrites MFe_2O_4 ($\text{M} = \text{Mg, Mn, Fe, Co, Ni, Cu, Zn}$) with tunable electromagnetic properties and strong microwave absorption. *J Adv Ceram.* 2022, 11: 754-768.
- [42] Liu X, Tian F, Sheng J, *et al.* High-entropy porous spinel ferrite @ amorphous carbon nanocomposites with abundant structural defects for wide-band electromagnetic wave absorption. *Chem. Eng. J.* 2024, 490: 151848.
- [43] Xu X, Li D, Li L, *et al.* Architectural Design and Microstructural Engineering of Metal–Organic

Framework - Derived Nanomaterials for Electromagnetic Wave Absorption. *Small Struct.* 2023, 4: 2200219.

[44] Tian F, Gao Y, Wang A, *et al.* Effect of Mn substitution on structural, magnetic and microwave absorption properties of Co₂Y hexagonal ferrite. *J. Magn. Magn. Mater.* 2023, 587: 171229.

[45] Liu Y, Li H, Yan X, *et al.* Ultra-broadband microwave absorption of (Mn_{0.2}Fe_{0.2}Zn_{1.2})_x substituted Co₂Y hexaferrites with a self-aligned sheet stacked, highly c-axis oriented and multi-domain structure. *J. Mater. Chem. A.* 2023, 11: 26285-26300.

[46] Ghosh K, Srivastava S K. Fabrication of N-Doped Reduced Graphite Oxide/MnCo₂O₄ Nanocomposites for Enhanced Microwave Absorption Performance. *Langmuir.* 2021, 37: 2213-2226.

[47] Luo X, Li H, Deng D, *et al.* Preparation and excellent electromagnetic absorption properties of dendritic structured Fe₃O₄@PANI composites. *J. Alloys Compd.* 2022, 891: 161922.

[48] Wang X Y, Wei S C, Wang B, *et al.* Doping sites, magnetic, and microwave absorption properties of barium ferrites with multiple magnetic resonances. *J. Mater. Sci-Mater. El.* 2023, 34: 16.

[49] Kitagawa R, Kohashi T, Tsuji T, *et al.* Wide-field imaging of the magnetization process in soft magnetic-thin film using diamond quantum sensors. *Appl. Phys. Express.* 2024, 17: 017002.

[50] Song L, Wu C, Zhi Q, *et al.* Multifunctional SiC aerogel reinforced with nanofibers and nanowires for high-efficiency electromagnetic wave absorption. *Chem. Eng. J.* 2023, 467: 143518.

[51] Yang J, Wen Q, Feng B, *et al.* Microstructural evolution and electromagnetic wave absorbing performance of single-source-precursor-synthesized SiCuCN-based ceramic nanocomposites. *J. Adv. Ceram.* 2023, 12: 1299-1316.

[52] Jiang X, Niu H, Li J, *et al.* Construction of core-shell structured SiO₂@MoS₂ nanospheres for broadband electromagnetic wave absorption. *Appl. Surf. Sci.* 2023, 628: 157355.

[53] Quan B, Liang X, Ji G, *et al.* Dielectric polarization in electromagnetic wave absorption: Review and perspective. *J. Alloys Compd.* 2017, 728: 1065-1075.

Open Access This article is licensed under a Creative Commons Attribution 4.0 International License, which permits use, sharing, adaptation, distribution and reproduction in any medium or format, as long as you give appropriate credit to the original author(s) and the source, provide a link to the Creative Commons licence, and indicate if changes were made.

The images or other third party material in this article are included in the article's Creative Commons licence, unless indicated otherwise in a credit line to the material. If material is not included in the article's Creative Commons licence and your intended use is not permitted by statutory regulation or exceeds the permitted use, you will need to obtain permission directly from the copyright holder.